Biosurface and Biotribology

WILEY

The Institution of Engineering and Technology

ORIGINAL RESEARCH OPEN ACCESS

Electrostatically Assembled HA–DN/AMSN–TCS Coatings for Antibacterial Urinary Catheters

Jiafeng Hu[1,2] | Xiaojun Chen[1,2] | Yingwei Chen[3] | Lin Wu[1,2] | Chengxiong Lin[1,2]

[1]Key Laboratory of Metallurgical Equipment and Control Technology, Ministry of Education, Wuhan University of Science and Technology, Wuhan, China | [2]Hubei Key Laboratory of Mechanical Transmission and Manufacturing Engineering, Wuhan University of Science and Technology, Wuhan, China | [3]School of Mathematics and Computer Science, Wuhan Polytechnic University, Wuhan, China

Correspondence: Lin Wu (wulin90@wust.edu.cn) | Chengxiong Lin (lcx3625@wust.edu.cn)

Received: 29 December 2025 | **Revised:** 14 April 2026 | **Accepted:** 21 April 2026

Keywords: adhesion and friction | antifungi | antimicrobial | biointerface | biological adhesion

ABSTRACT

Catheter-associated urinary tract infections (CAUTIs) are a significant complication of indwelling urinary catheters, primarily caused by bacterial adhesion, biofilm formation and catheter-induced mechanical irritation. To reduce the risk of infection and enhance catheter safety and performance, this study developed an antibacterial lubricating coating. The coating was fabricated on a polytetrafluoroethylene (PTFE) substrate via electrostatic self-assembly, combining dopamine-modified hyaluronic acid–dopamine (HA–DN) as a biomimetic adhesive with aminated mesoporous silica nanoparticles (AMSN) serving as a long-acting drug delivery carrier loaded with triclosan (TCS). The results demonstrated that the prepared AMSN exhibited a uniform particle size of approximately 80 nm, an ordered mesoporous structure and a high drug-loading capacity, enabling sustained in vitro release of TCS for up to 144 h. Additionally, the composite multilayer coating significantly improved surface hydrophilicity and lubricity, exhibited strong antibacterial activity against *Escherichia coli* and *Staphylococcus aureus* and maintained good biocompatibility. These findings highlight its potential for preventing CAUTIs and enhancing the safety of indwelling urinary catheters.

1 | Introduction

Catheter-associated urinary tract infection (CAUTI) remains one of the most common and challenging hospital-acquired infections, accounting for approximately 30%–40% of nosocomial infections and ranking second only to respiratory tract infections. Epidemiological evidence suggests that 75%–80% of urinary tract infections are associated with indwelling urinary catheters [1, 2]. CAUTI is driven by multiple factors, including urethral mucosal injury during catheterisation, bacterial ascension through extraluminal and intraluminal routes, biofilm formation and catheter encrustation, inappropriate catheter materials and irrigation practices, irrational antibiotic use, as well as host susceptibility factors such as impaired immunity and comorbidities (e.g., benign prostatic hyperplasia and diabetes). Once established, the infection can impair catheter function and may progress to severe systemic complications. Therefore, beyond standardised catheter care, engineering catheter surfaces with enhanced antibacterial and antifouling properties is a key strategy to reduce CAUTI and improve clinical outcomes.

Current anti-CAUTI catheter designs primarily target early stages of infection—such as bacterial adhesion, biofilm maturation and encrustation—using chemical and physical surface modification strategies [3]. Chemically modified systems incorporate antibacterial agents including functional polymers, antibiotics, antimicrobial peptides, bacteriophages or enzyme inhibitors [4]. Antibiotics remain the most widely used agents

clinically, although many alternative bioactive compounds are still under investigation [5–8]. However, coatings that rely on a single bactericidal mechanism often exhibit limited durability and may promote resistance and biosafety concerns, underscoring the need to balance long-term efficacy with toxicity and antimicrobial stewardship [9, 10]. In parallel, physical modifications—particularly hydrophilic and lubricious coatings—reduce catheter–tissue friction and mechanical irritation, thereby decreasing initial bacterial attachment and subsequent biofilm development [11]. Typical hydrophilic coatings (e.g., PVP, poly(MPC-co-BMA), ammonium polyacrylate and commercial lubricious coatings) have been shown to reduce bacterial adhesion, encrustation and crystalline deposits such as struvite and hydroxyapatite) [12–15]. Nonetheless, many catheter coatings still face practical challenges, especially insufficient antibacterial durability and coating instability or detachment under prolonged physiological and mechanical stresses [16–18].

In our previous work, we developed an antibacterial coating by integrating PLGA-based drug-loaded microspheres within a chitosan-modified gel matrix, which enhanced antibacterial stability via dual-drug delivery [19]. However, microscale components may detach or degrade under physiological conditions, prompting the development of more stable nanoscale coating architectures. Mesoporous silica nanoparticles (MSNs), characterised by a high surface area and tunable pore structures, are attractive sustained-release carriers that can protect payloads from premature degradation and enable prolonged, controllable release [20]. Here, we propose a multifunctional catheter coating that combines long-term antibacterial activity with enhanced lubrication by integrating a bio-inspired adhesive/hydrophilic layer—dopamine-modified oxidised hyaluronic acid—with an aminated MSN-based sustained-release platform. The coating is constructed on polyurethane substrates via electrostatic self-assembly, followed by Schiff base cross linking, forming a stable interfacial network [21]. This design aims to (i) provide prolonged antibacterial release to suppress bacterial adhesion and biofilm formation while reducing resistance pressure and (ii) enhance surface hydrophilicity and lubricity to minimise urethral irritation during insertion and indwelling use, thereby offering a promising approach toward safer and more durable next-generation urinary catheters (Figure 1).

Recently, remarkable advances have been achieved in antimicrobial coatings, bioinspired adhesion strategies, and catheter–tissue interface friction. Pu et al. explored the fretting corrosion behaviour of CoCrMo–Ti6Al4V alloy pairs under inflammatory environments [22] and revealed the fretting corrosion mechanisms of Ti6Al4V against CoCrMo in simulated body fluid [23]; they also summarised the tribocorrosion progress of metallic biomaterials under inflammatory conditions [24]. Lin et al. established a quantitative friction–damage model for intervention catheter–vascular tissue interfaces [16] and developed lubricating nano-coatings for cardiovascular catheters via molecular self-assembly and Schiff base reaction [17]. Yuan et al. reviewed the interaction between blood vessels and interventional catheters as well as related surface modification advances [25]. In addition, bioinspired self-adhesive lubricious antibacterial coatings for medical devices [26] and hydrophilic antibacterial lubricating coatings for urinary tract implants [27] have been widely developed. Different from single-function coatings, this work integrates electrostatic self-assembly, biomimetic HA–DN adhesion, and AMSN–TCS sustained-release system to achieve simultaneous lubrication and long-term antibacterial activity, making it more suitable for high-safety urinary catheter applications.

2 | Materials and Methods

2.1 | Preparation of Aminated Mesoporous Silica and Subsequent Drug Loading

Aminated mesoporous silica (AMSN) was prepared using a silane coupling agent grafting method, followed by loading TCS through physical adsorption [28, 29]. 0.81 g of (3-aminopropyl)triethoxy silane (APTES, 97 wt%) was dissolved in 15.8 g of anhydrous ethanol, and the mixture was stirred at room temperature to form a homogeneous solution. Add 0.5 g of pretreated, dried mesoporous silica (MCM-41) to the above solution and stir continuously to achieve uniform dispersion. Stir the mixture at room temperature for 24 h to fully graft the silane coupling agent to the silica surface. After the reaction, wash the mixture several times with anhydrous ethanol to remove unreacted APTES and by-products. Filter the suspension, and dry the resulting precipitate in a drying oven to obtain AMSN. Prepare TCS solutions by dissolving 200 mg or 400 mg of TCS in 40 mL of anhydrous ethanol, respectively. Mix each TCS solution with 400 mg of AMSN and sonicate for 5 min to ensure uniform dispersion. The reaction system was stirred at room temperature for 4 h to ensure complete drug loading. After the reaction, the mixture was centrifuged to collect the precipitate. The supernatant was discarded, and the obtained drug-loaded AMSN samples were designated as AMSN/0, AMSN/200 and AMSN/400, corresponding to the respective drug loading concentrations.

2.2 | Preparation of HA–DN

The HA–DN conjugate was synthesised via a carbodiimide-mediated coupling reaction between hyaluronic acid (HA) and dopamine hydrochloride. Forty milligrams of HA powder were dispersed in 8 mL of phosphate-buffered saline (PBS), and the pH of the solution was adjusted to 5.0 using dilute hydrochloric acid. Subsequently, 13.5 mg of N-(3-dimethylaminopropyl)-N′-ethylcarbodiimide hydrochloride (EDC) and 19 mg of dopamine hydrochloride were added to the reaction mixture. The coupling reaction was conducted under a nitrogen atmosphere at 25°C for 5 h with continuous stirring. After the reaction, the resulting solution was transferred to a dialysis membrane with a molecular weight cut-off of 3500 Da for purification. Dialysis was performed against deionised water adjusted to pH 5.0, with the dialysis medium replaced every 3 h over a 72-h period to remove unreacted reagents and low-molecular-weight impurities. After purification, the dialysed solution was frozen at −20°C and subsequently freeze-dried to obtain the HA–DN conjugate as a solid powder. The final product was sealed and stored in a dry environment for subsequent experiments.

2.3 | Preparation of Drug-Loaded Coating

An oxidative cleaning solution was prepared by mixing equal volumes of ammonia solution and hydrogen peroxide. PTFE substrates were immersed in this solution and subjected to

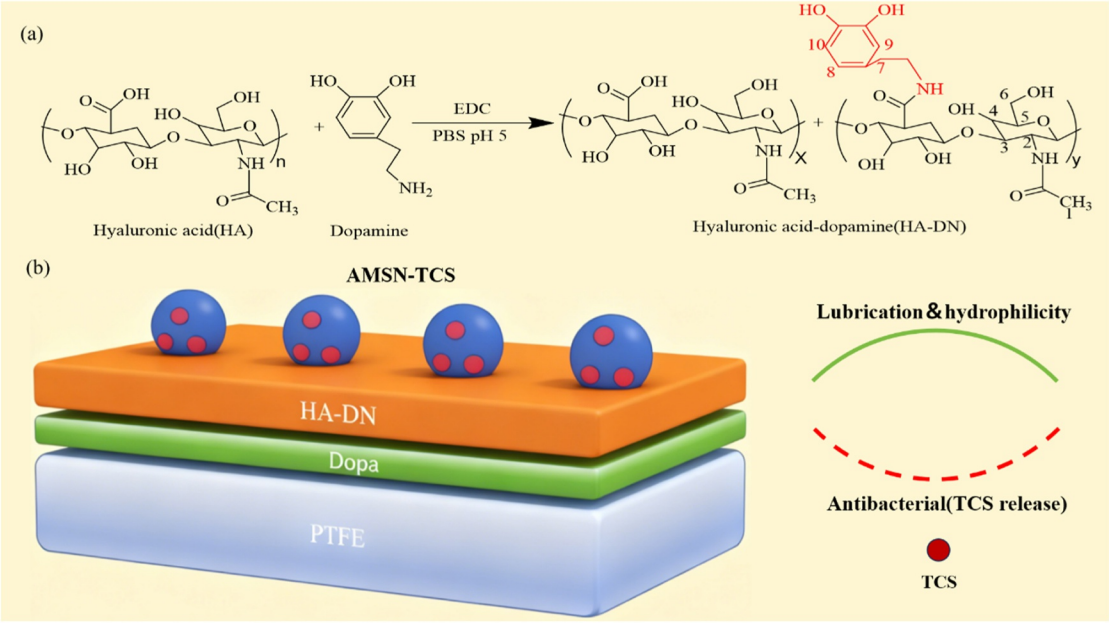

FIGURE 1 | (a) EDC-mediated conjugation of hyaluronic acid (HA) with dopamine to form HA–DN in PBS (pH 5). (b) Schematic of an AMSN–TCS–loaded HA–DN coating on PTFE, providing enhanced hydrophilicity/lubrication and antibacterial activity via TCS release.

oscillatory stirring for 20 min, followed by sequential rinsing with triple-stage deionised water and drying under a nitrogen flow. Subsequently, the cleaned substrates were immersed in a dopamine hydrochloride solution (2 mg/mL) and continuously shaken at 25°C for 4 h to form a polydopamine interlayer. The samples were then ultrasonically cleaned in ultrapure water for 15 min and dried again under a nitrogen stream. The polydopamine-modified substrates were immersed in a dopamine-modified hyaluronic acid–dopamine gel (HA–DN, 1 mg/mL) for 15 min to deposit a lubricious adhesive layer. After rinsing with deionised water, a stable adhesive-lubricating coating was obtained. To impart antibacterial functionality, the HA–DN–coated substrates were immersed in 10 mL of a pre-prepared triclosan-loaded ANMSN dispersion for 15 min. After rinsing with deionised water for 5 min, antibacterial-lubricating composite coatings were successfully formed.

By controlling the drug-loading content, three types of composite coatings—designated as PTFE/0, PTFE/200, and PTFE/400—were produced. Multilayer drug-loaded AMSN coatings were subsequently fabricated on PTFE substrates by alternately immersing them in HA–DN and drug-loaded AMSN solutions. Pristine PTFE substrates without HA–DN or AMSN modifications were used as the control group and retained their intrinsic polymer properties.

2.4 | Characterization of Physicochemical Properties of Coating Materials

The microstructural characteristics of mesoporous silica nanoparticles and their composite coatings were examined using scanning electron microscopy (SEM, Sigma 300, Carl Zeiss, Germany), with particular emphasis on particle morphology and pore structure [30–33]. Prior to observation, the samples were ultrasonically dispersed in anhydrous ethanol to ensure uniform dispersion, and the suspension concentration was adjusted to 0.5–1 mg/mL. The dispersed suspension was then uniformly deposited onto the surface of a copper grid substrate and allowed to dry naturally in a constant-temperature environment. SEM was subsequently employed to obtain three-dimensional nanoscale structural information of the mesoporous silica nanoparticles [34]. After coating, SEM was further used to characterize PTFE substrates coated with 2, 4 and 6 layers, and their surface morphologies were compared with that of the untreated PTFE substrate to evaluate the influence of different coating layers on surface morphology [35].

Thermogravimetric analysis (TGA) was conducted to assess the thermal stability of the materials by monitoring their mass variation under controlled temperature conditions. Specifically, 3–5 mg of each sample (MSN, AMSN, AMSN/200, AMSN/400 and TCL) was placed in an alumina crucible and heated from 0°C to 800°C at a rate of 10°C/min under a nitrogen atmosphere with a flow rate of 50 mL/min. During the heating process, a high-precision balance continuously recorded real-time mass changes as a function of temperature, enabling analysis of the effects of surface modification and drug loading on the thermal stability of the materials.

XPS and Fourier-transform infrared spectroscopy (FTIR, Nicolet iS50, Thermo Fisher Scientific, USA) were employed to characterize the surface modification and drug loading of the nanoparticles [36]. For FTIR analysis, MSN, AMSN, AMSN/200, AMSN/400 and TCL samples were finely ground and mixed with KBr to achieve submicron dispersion. The resulting mixtures were transferred into a standard mold and pressed into thin pellets under a pressure of 10 MPa. The FTIR spectra of the prepared pellets were then recorded to analyse the molecular structure and surface chemical characteristics of the samples.

Zeta potential measurements were performed to evaluate the surface charge properties of the mesoporous silica nanoparticles [37]. In this experiment, 5 mg of each sample was dispersed in 10 mL of ultrapure water and ultrasonicated to obtain a

homogeneous suspension. The zeta potential was subsequently measured at 25°C using a phase analysis light scattering (PALS) zeta potential analyser to determine the surface charge distribution and colloidal stability of the nanoparticles.

Nitrogen adsorption–desorption analysis was carried out to characterize the pore structure of the porous materials [38]. Based on gas adsorption theory, the nitrogen adsorption capacity of the samples was measured at a low temperature by varying the relative pressure (p/p_0), and adsorption–desorption isotherms were obtained [39]. The specific surface area was calculated using the Brunauer–Emmett–Teller (BET) method, whereas the pore size distribution was determined using the Barrett–Joyner–Halenda (BJH) model, allowing further evaluation of structural parameters such as pore volume.

The drug release behaviour of the drug-loaded mesoporous silica materials was evaluated using the dialysis method [40]. Initially, triclosan ethanol solutions of varying concentrations were prepared to establish a standard calibration curve. Subsequently, 40 mg of AMSN/200 and AMSN/400 samples were dispersed in 40 mL of a 20% ethanol solution and sealed in dialysis bags with a molecular weight cut-off of 3500 Da. The dialysis bags were then placed in a shaker for continuous release testing. During the release process, aliquots were collected at 4-h intervals to determine the triclosan concentration in the release medium. Finally, cumulative drug release profiles were plotted to analyse the release characteristics of the drug-loaded mesoporous silica materials.

2.5 | Antibacterial Performance Evaluation

In this experiment, the research team selected three composite materials with a four-layer coating structure: PTFE/0, PTFE/200 and PTFE/400. *Escherichia coli* (EC) and *Staphylococcus aureus* (SA) were used as test microorganisms to evaluate antibacterial performance. The experiment involved both qualitative analysis of inhibition zones and quantitative measurement of bacterial growth inhibition.

First, the prestored *Escherichia coli* and *Staphylococcus aureus* bacterial solutions were activated. The procedure was as follows: 1 mL of bacterial solution was added to 10 mL of the broth medium, and the culture was incubated for 24 h until the bacterial concentration reached the logarithmic growth phase. Then, each composite material (PTFE/0, PTFE/200 and PTFE/400) was placed in the centre of a petri dish containing the bacterial solution, and the dish was incubated at 37°C for 24 h. After incubation, the materials were removed from the petri dish, and images of the inhibition zones were captured using a camera. Finally, the diameter of the inhibition zones was measured and recorded to evaluate the antibacterial activity of the composite materials.

To further quantify the antibacterial effect, the experiment was conducted as follows: First, prestored *Escherichia coli* and *Staphylococcus aureus* bacterial solutions were activated. Each of the four 1-mL aliquots of bacterial solution were added to 10 mL of the broth medium. The first served as a blank control, whereas the second, third and fourth were mixed with equal amounts of PTFE/0, PTFE/200 and PTFE/400 samples, respectively, for co-culture. All samples were incubated at 37°C in a constant-temperature incubator for 24 h.

After incubation, 1 mL of the culture medium was collected and centrifuged to separate the liquid from the bacterial pellet. The pellet was then resuspended in 1 mL of sterile deionised water, and an appropriate volume of this diluted suspension was transferred to a 96-well plate. The optical density (OD) at 610 nm was measured to determine the bacterial concentration in the sample, which was used to evaluate the antibacterial effect of the materials. All quantitative assessments were conducted in triplicate ($n = 3$) independent experiments. Data are presented as mean ± standard deviation (SD). Statistical analysis was performed using one-way ANOVA, and a p-value < 0.05 was considered to indicate statistical significance.

3 | Physicochemical Properties of Coating Materials

3.1 | Surface Morphology

The surface morphology and pore structure of the mesoporous silica are illustrated in Figure 2. Scanning electron microscopy (SEM) images reveal that the mesoporous silica particles exhibit a star-like morphology, with an average particle size of approximately 80 nm and a narrower size distribution. These particles possess a well-defined internal structure composed of densely packed, ordered pore channels. The high density of these mesoporous channels significantly increases the specific surface area and pore volume, thereby providing ample space for TCS loading. As shown in Figure 2, the surface of the untreated PTFE substrate displays numerous deep pits. With an increasing number of coating layers, these surface pits are gradually filled, accompanied by a progressive increase in the coverage of mesoporous silica particles. This evolution in surface morphology is advantageous for reducing the friction coefficient at the interface between the device and human tissue, which is expected to mitigate the risk of clinical adverse reactions caused by frictional irritation.

3.2 | Thermal Stability

The TGA curves of mesoporous silica, aminated mesoporous silica and aminated mesoporous silica with varying drug loadings are presented in Figure 3. As shown, plain mesoporous silica demonstrates strong thermal stability, with minimal mass loss—primarily due to water evaporation—over the temperature range from 0°C to 800°C. This stability is attributed to the inherent high-temperature resistance of silica. In contrast, the mass loss of aminated mesoporous silica increases significantly because the amine groups from APTES molecules are chemically grafted onto the mesoporous silica surface during the amination process. These organic groups exhibit poor thermal stability and undergo substantial decomposition upon heating. Furthermore, as the drug loading increases, the mass loss intensifies due to the combined thermal decomposition of triclosan, which acts as an organic carrier, and the amine groups. These results confirm the successful amination of mesoporous silica. Additionally, the mass loss observed in drug-loaded mesoporous silica is lower than that of aminated mesoporous silica without drug, indicating that although drug loading was

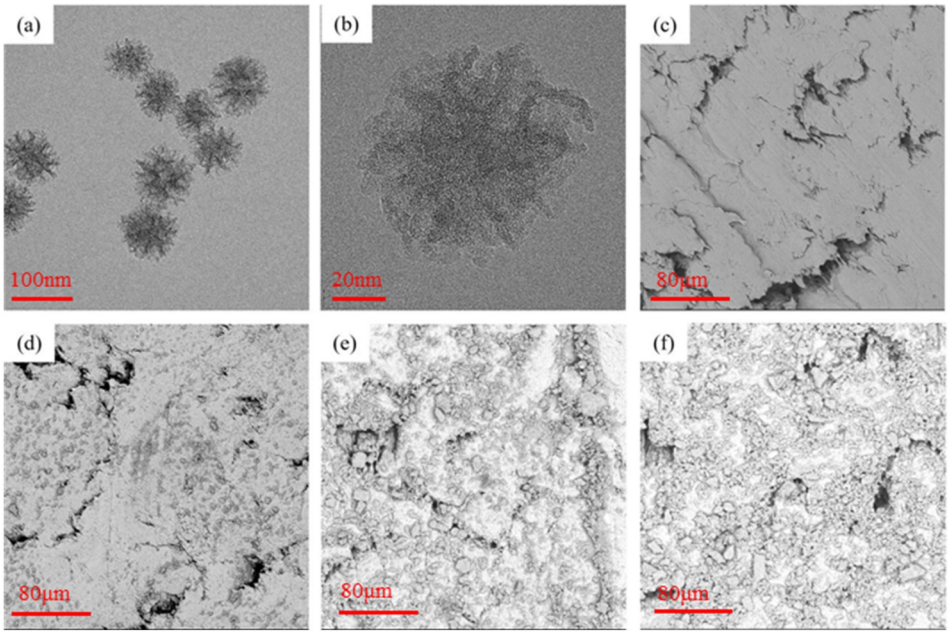

FIGURE 2 | Morphology of mesoporous silica and coated PTFE surfaces. (a) TEM: star-like mesoporous silica nanoparticles (~80 nm). (b) TEM (high magnification): ordered mesoporous channels within a single particle. (c) SEM: untreated PTFE with deep surface pits. (d–f) SEM: PTFE with 1, 2 and 3 coating layers, showing progressive pit filling and increased particle coverage. Scale bars: (a) 100 nm, (b) 20 nm and (c–f) 80 μm.

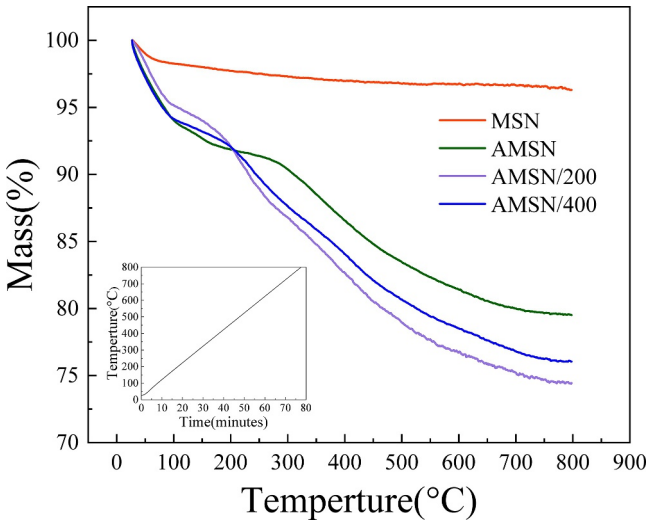

FIGURE 3 | TGA curves (0°C–800°C) of DMSN, ADMSN and triclosan-loaded ADMSN (ADMSN/200 and ADMSN/400).

successful, the change in mass loss does not significantly reflect the amount of drug loaded.

3.3 | X-Ray Photoelectron Spectroscopy (XPS) Analysis

The XPS analysis results of mesoporous silica, AMSN and aminated mesoporous silica with varying drug loadings are presented in Figure 4. The analysis primarily focuses on the chlorine peak, with a binding energy around 198–199 eV, and the nitrogen peak, around 398–406 eV. The results indicate that no chlorine was detected in the MSN and AMSN samples, whereas characteristic chlorine peaks were observed in the TCS, AMSN/200 and AMSN/400 samples. This chlorine originates from triclosan (TCS, molecular formula C12H7Cl3O2), directly confirming that AMSN successfully loaded triclosan. Furthermore, no nitrogen peaks were observed in the TCS and MSN samples, but a prominent nitrogen peak appeared in the aminated materials. This is due to the amino (-NH2) modification on the surface of mesoporous silica, further verifying the successful aminisation of mesoporous silica.

3.4 | Fourier-Transform Infrared Spectroscopy (FTIR)

The characteristic infrared absorption peaks of mesoporous silica and triclosan are summarised in the simplified Table 1. The FTIR spectra of MSN, AMSN, AMSN/200, AMSN/400 and TCS are presented in Figure 5. Spectral analysis reveals that the drug-loaded mesoporous silica exhibits no significant differences from the unloaded samples in the fingerprint region below 1350 cm^{-1}. In this region, mesoporous silica primarily shows bands at 3450 cm^{-1} (O–H stretching), 1630 cm^{-1} (H–O–H bending of adsorbed water), 1080–1250 cm^{-1} (Si–O–Si asymmetric stretching), 800–850 cm^{-1} (Si–O–Si symmetric stretching) and 950–970 cm^{-1} (Si–OH bending). In contrast, the region above 1350 cm^{-1} corresponds to the functional group region, where triclosan exhibits distinct absorption bands at 1600, 1580 and 1450 cm^{-1}, arising from the aromatic C=C skeletal vibrations of the benzene ring, along with bands at 3060–3100 cm^{-1} for aromatic C–H stretching and 3000–3500 cm^{-1} for O–H stretching. Compared with MSN and AMSN, these characteristic peaks are clearly detected in the spectra of AMSN/200 and AMSN/400, demonstrating the successful loading of triclosan into the aminated mesoporous silica. These characteristic peaks identified in FTIR spectra are highly consistent with the chemical structure and bonding information of the HA–DN conjugate and AMSN–TCS illustrated in Figure 1a, clearly confirming the successful synthesis of the

designed coating structure and the rationality of the molecular assembly route. Moreover, because the fingerprint region below 1350 cm^{-1} is highly sensitive to molecular structural variations, the absence of notable spectral changes before and after drug incorporation further suggests that triclosan is accommodated within the mesoporous silica primarily through intermolecular interactions, without inducing significant structural alterations to the silica framework.

3.5 | Zeta Potential Analysis

The zeta potentials of MSN, AMSN, AMSN/200, AMSN/400 and TCS are presented in Figure 6. As shown, the unmodified mesoporous silica exhibits a negative zeta potential, which is unfavorable for electrostatic adsorption with HA–DN due to the similarly negative surface charge of HA–DN. In contrast, after amination, the surface charge of mesoporous silica reverses to a positive zeta potential and remains positive following drug loading, thereby satisfying the essential conditions for electrostatic assembly. Previous studies have also reported that aminated mesoporous silica generally exhibits a positive zeta potential. These results are consistent with the literature, further confirming the effectiveness of the amination modification.

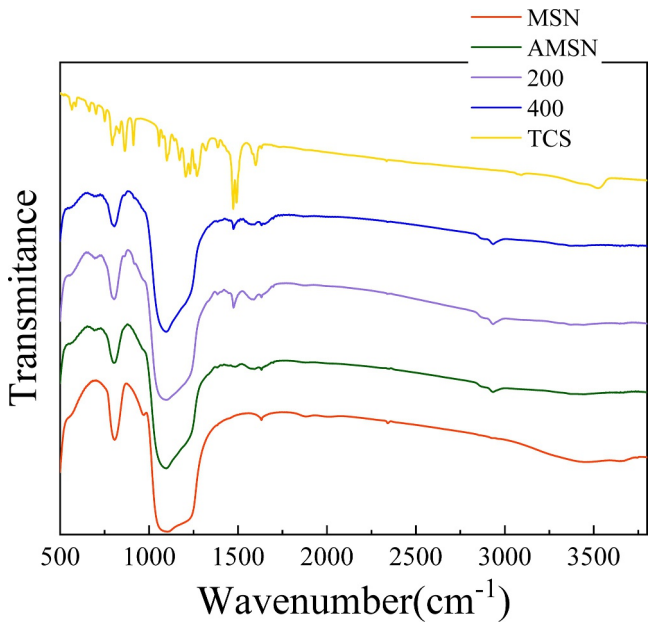

FIGURE 5 | FTIR spectra of MSN, AMSN, triclosan-loaded AMSN (AMSN/200 and AMSN/400) and triclosan (TCS) in the range of 500–3600 cm^{-1}.

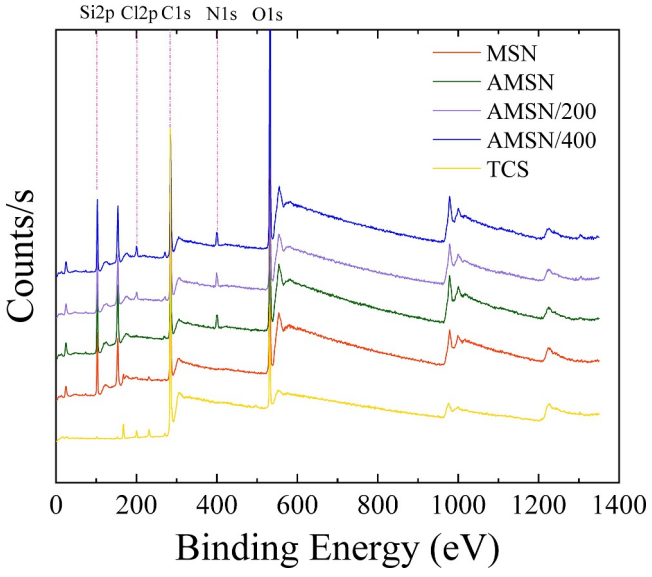

FIGURE 4 | XPS survey spectra of MSN, AMSN, AMSN/200, AMSN/400 and TCS over the binding energy range of 0–1400 eV, with marked regions corresponding to Si2p, Cl2p, Cls, N1s and O1s.

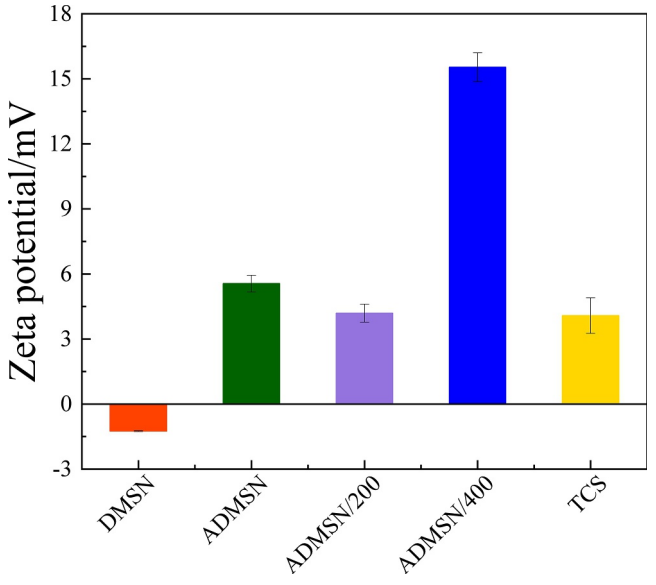

FIGURE 6 | Zeta potentials of DMSN, ADMSN, ADMSN/200, ADMSN/400 and TCS (mean ± SD).

TABLE 1 | Characteristic FTIR absorption peaks of mesoporous silica and triclosan.

Number	O–H stretching (cm^{-1})	Si–O–Si stretching (cm^{-1})	Si–OH bending (cm^{-1})	Aromatic C=C (cm^{-1})
MSN	~3450	1080–1250	~960	—
AMSN	~3450	1080–1250	~960	—
AMSN/200	~3450	1080–1250	~960	1600, 1580 and 1450
AMSN/400	~3450	1080–1250	~960	1600, 1580 and 1450
TCS	3000–3500	—	—	1600, 1580 and 1450

3.6 | Nitrogen Adsorption–Desorption Analysis

Activated carbon is a well-known porous material with a typical specific surface area in the range of 500–1500 m^2/g. As summarised in Table 2, the specific surface area of mesoporous silica is comparable to that of activated carbon, indicating that mesoporous silica also possesses a high surface area and is therefore favorable for drug loading. After amination, a pronounced decrease in specific surface area accompanied by an increase in pore size is observed; nevertheless, the material still retains a considerable drug-loading capability. The AMSN exhibit a pore volume of 1.07 cm^3/g and an average pore diameter of 23.78 nm, which is well matched to the size of many drug molecules and thus conducive to achieving high encapsulation efficiency of antimicrobial agents. Notably, no significant change in pore size is detected after drug loading, suggesting that the incorporation of drugs occurs mainly through intermolecular interactions and pore filling, whereas the mesoporous framework remains intact, demonstrating good structural stability.

3.7 | Hydrophilicity Angle Measurement

The water contact angle results are presented in Figure 7. The pristine PTFE substrate (control) exhibited a contact angle of approximately 108°, indicating a hydrophobic surface ($\theta > 90°$). As the number of coating layers increased, the contact angle progressively decreased. After applying four layers, the contact angle dropped to about 60°, indicating a transition to a hydrophilic surface ($\theta < 90°$). This trend suggests that the multilayer coating effectively enhances surface wettability, consistent with the intended lubrication design. Although drug loading caused a slight increase in the contact angle, the change was minimal, and the coated surface still maintained good lubricity.

4 | Antibacterial Performance Test

4.1 | Antibacterial Performance Test by the Inhibition Zone Method

The inhibition zone assay results for PTFE/0, PTFE/200 and PTFE/400 against *Escherichia coli* and *Staphylococcus aureus* are presented in Figure 8. No inhibition zone was observed for the control sample PTFE/0, indicating that the mesoporous silica matrix itself does not exhibit antibacterial activity. In contrast, both PTFE/200 and PTFE/400 demonstrated pronounced antibacterial effects against the tested strains. As the TCS content increased, the inhibition zone diameter also increased, reflecting enhanced antibacterial efficacy. These results indicate that TCS loaded into mesoporous silica can be effectively released even under nonsolution conditions, enabling the coating to maintain reliable antibacterial performance in practical applications. However, the inhibition zone of PTFE/400 did not show a significant increase compared to that of PTFE/200. This phenomenon may be attributed to saturation of the drug-loading capacity of the modified mesoporous silica, beyond which further increases in TCS content do not result in proportional improvements in antibacterial performance.

4.2 | Bacterial Concentration Measurement

Figure 9 illustrates the variation in bacterial concentration on PTFE/0, PTFE/200 and PTFE/400 samples during coculture with bacteria over a 144-h period. The bacterial concentration on the TCS-loaded PTFE samples was significantly lower than that on the control sample (PTFE/0), demonstrating the effective incorporation of TCS into the coating. Furthermore, the results indicate that the antibacterial coating continuously suppressed bacterial proliferation throughout the 144-h incubation period, confirming its sustained antibacterial activity and long-term stability.

5 | Conclusion

To address catheter-associated urinary tract infections (CAUTIs) associated with indwelling urinary catheters, this study developed and evaluated an antibacterial and lubricating HA–DN/AMSN composite coating on PTFE substrates. The coating combines dopamine-modified hyaluronic acid with drug-loaded mesoporous silica nanoparticles to enhance surface hydrophilicity and lubricity while providing sustained antibacterial activity. Furthermore, considering the mechanical friction

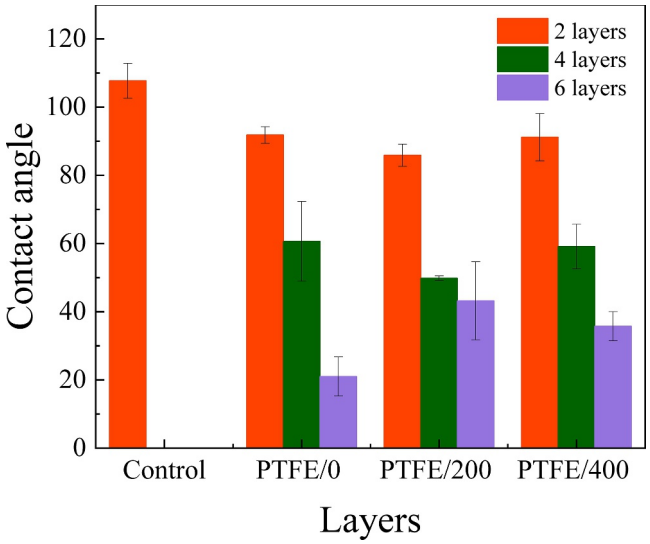

FIGURE 7 | Water contact angle (°) of the pristine PTFE substrate (control) and coated samples with different drug loadings (PTFE/0, PTFE/200 and PTFE/400) at different coating layer numbers (2, 4 and 6 layers).

TABLE 2 | Specific surface area, pore volume and pore size of mesoporous silica.

Number	Surface area	Pore volume (P/Po = 0.99)	Pore size (adsorption)	Pore size (desorption)
MSN	477.0460	1.615908	15.3439	15.0075
AMSN	170.7999	1.076309	23.7861	24.1276
AMSN/200	150.0108	0.960678	24.2931	24.1276
AMSN/400	150.5047	0.947994	24.9586	23.5247

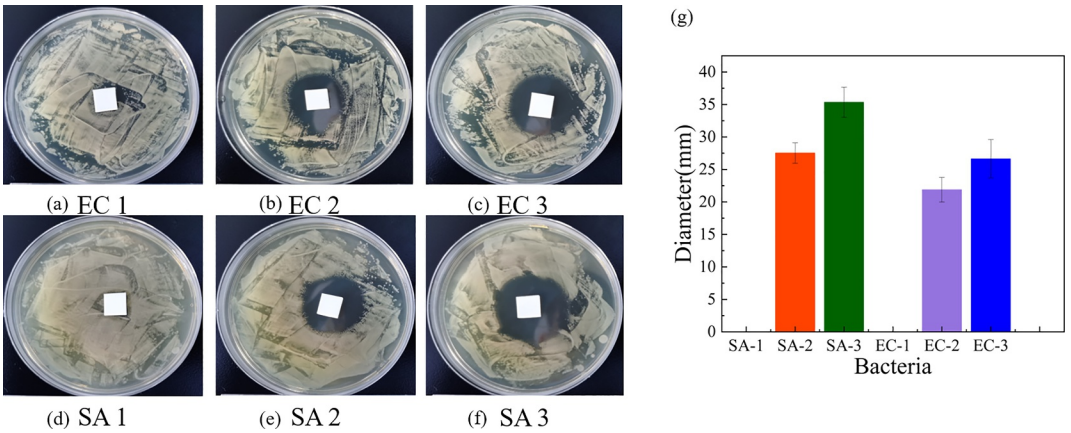

FIGURE 8 | Inhibition zone assay of PTFE samples with different TCS loadings (PTFE/0, PTFE/200 and PTFE/400) against *Escherichia coli* and *Staphylococcus aureus*. (a–c) Representative agar plates for *E. coli* (EC-1 to EC-3), (d–f) representative agar plates for *S. aureus* (SA-1 to SA-3) and (g) corresponding inhibition zone diameters (mm).

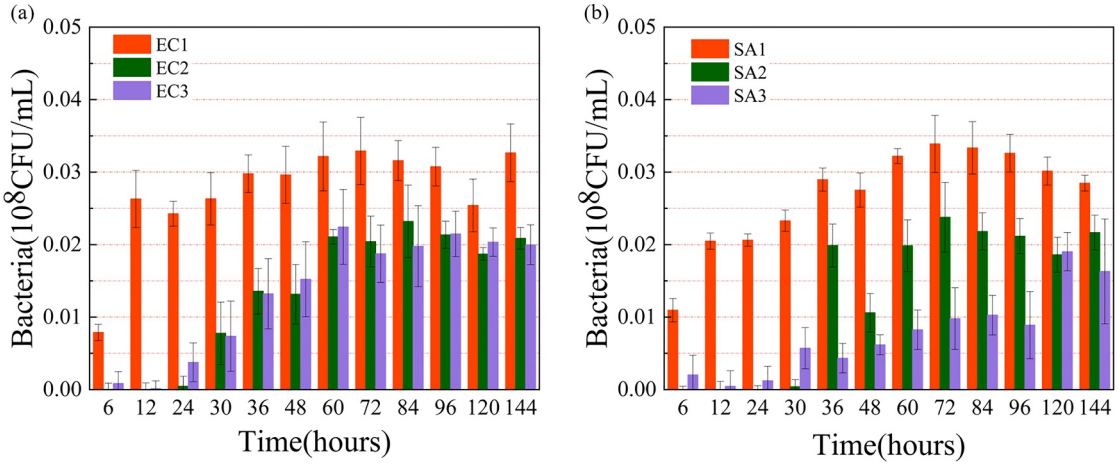

FIGURE 9 | Time-dependent bacterial concentration (× 10^8 CFU/mL) on PTFE samples with different TCS loadings (PTFE/0, PTFE/200 and PTFE/400) during the 144-h co-culture. (a) *Escherichia coli*. (b) *Staphylococcus aureus*. Bars represent mean values, and error bars indicate standard deviation.

between the catheter and urethral tissue in the physiological environment, the lubrication durability of the coating under dynamic friction conditions and its protective effect on soft tissue will be taken into account in future research, which is helpful to reduce tissue irritation and infection risk. Overall, the results indicate that the coating can be stably applied to PTFE and shows potential to reduce bacterial colonisation and improve catheter performance. The main conclusions are as follows:

1. AMSN were synthesised using a silane coupling agent grafting method. The resulting nanoparticles exhibited a uniform particle size of approximately 80 nm and an ordered mesoporous structure, with a pore volume of 1.07 cm^3/g and an average pore diameter of 23.78 nm, resulting in high drug-loading capacity. Triclosan (TCS)-loaded AMSN demonstrated sustained in vitro release for up to 144 h.

2. Dopamine-modified hyaluronic acid (HA–DN) facilitated the stable immobilisation of drug-loaded AMSN onto the PTFE surface through electrostatic self-assembly. As the number of coating layers increased, the composite coating progressively filled the surface defects of the PTFE substrate, forming a uniform and stable structure that significantly enhanced surface hydrophilicity and lubricity.

3. The HA–DN/AMSN composite coating demonstrated effective antibacterial activity against *Escherichia coli* and *Staphylococcus aureus*, maintaining efficacy for 144 h, while preserving favorable biocompatibility. This indicates its potential to reduce the risk of CAUTI and improve the performance of indwelling urinary catheters.

Funding

This research was funded by the National Natural Science Foundation of China (52205186).

Conflicts of Interest

The authors declare no conflicts of interest.

Data Availability Statement

The raw data supporting the conclusions of this article will be made available by the authors on request.

References

1. P. M. Latthe and A. M. Latthe, "Catheter-Associated Urinary Tract Infections—A Review," *Wadia Journal of Women and Child Health* 3 (2024): 79–82, https://doi.org/10.25259/wjwch_39_2024.

2. T. M. Waters, M. J. Daniels, G. J. Bazzoli, et al., "Medicare's Hospital-Acquired Conditions Policy," *JAMA Internal Medicine* 175, no. 3 (2015): 347, https://doi.org/10.1001/jamainternmed.2014.5486.

3. S. P. Subianto and P. D. Endraswari, "Fungal Colonization in Urinary Catheters: Pathophysiology and Clinical Implication," *International Journal Of Scientific Advances* 5, no. 6 (2024), https://doi.org/10.51542/ijscia.v5i6.0120.

4. L. Liu, B. Xue, M. Niu, et al., "Recent Advances in Anti-Infective Catheters for Preventing Catheters Associated Urinary Tract Infections," *Chemical Engineering Journal* 499 (2024): 156333, https://doi.org/10.1016/j.cej.2024.156333.

5. J. Wu, J. Yan, S. Xu, et al., "Novel Nano Drug-Loaded Hydrogel Coatings for the Prevention and Treatment of CAUTI," *Advanced Healthcare Materials* 13, no. 30 (2024): 2401745, https://doi.org/10.1002/adhm.202401745.

6. B. Sezer, E. Bilgi, G. Pulat, et al., "Development of Antimicrobial Peptide Conjugated PVC Catheters for Prevention of Catheter Associated Urinary Tract Infections," in *2024 Medical Technologies Congress (TIPTEKNO)* (2024), 1–4, https://doi.org/10.1109/TIPTEKNO63488.2024.10755408.

7. P. Roy, R. Saha, J. Pawlik, et al., "Cobalt Containing Antimicrobial Bioactive Glass Coated Urinary Catheter Towards Management of Catheter Associated Urinary Tract Infection (CAUTI): Significant In Vitro Characterizations," *Ceramics International* 50, no. 7 (2024): 11625–11638, https://doi.org/10.1016/j.ceramint.2024.01.065.

8. D. Patil, S. Aravindan, A. Pal, et al., "Microtopographic Superhydrophobic Polymer Surface to Prevent Urinary Tract Infections Causing Nosocomial Drug-Resistant Bacterial Adhesion," *Surfaces and Interfaces* (2023): 41, https://doi.org/10.1016/J.SURFIN.2023.103239.

9. D. Patra, S. Ghosh, S. Mukherjee, Y. Acharya, R. Mukherjee, and J. Haldar, "Antimicrobial Nanocomposite Coatings for Rapid Intervention Against Catheter-Associated Urinary Tract Infections," *Nanoscale* 16, no. 23 (2024): 17–11125, https://doi.org/10.1039/d4nr00653d.

10. M. Jia, H. Tan, Z. Liu, J. Wu, X. Gou, and J. An, "Polydopamine Nanoplatform for Synergistic Photothermal and Antibiotic Treatment of Catheter-Associated Urinary Tract Infection," *ACS Applied Nano Materials* 8, no. 27 (2025): 13851–13860, https://doi.org/10.1021/acsanm.5c02488.

11. R. Jiang, X. Y. Liu, S. Gao, et al., "A Scalable and Universal Strategy for Constructing Long-Term Antibacterial Coatings With Lubricant Property on Medical Catheters," *Progress in Organic Coatings* 196 (2024): 10, https://doi.org/10.1016/j.porgcoat.2024.108738.

12. F. Wang, W. Peng, D. Huo, et al., "Cu2xS Homojunction Coatings Empower Titanium Implants With Near-Infrared-Triggered Antibacterial and Antifouling Properties," *Journal of Materials Chemistry B: Materials for Biology and Medicine* 12, no. 24 (2024): 13, https://doi.org/10.1039/D4TB00235K.

13. F. Oustadi, E. D. Stephens, and M. Badv, "One-Pot Fabrication of Highly Flexible Fluorine-Free Lubricant-Infused Poly(Vinyl Alcohol) Films With Superior Antifouling Properties," *ACS Applied Materials and Interfaces* 49 (2024): 16, https://doi.org/10.1021/ACSAMI.4C16080.

14. T. Bompotis, E. Karastergiou, K. Giannakopoulos, et al., "Solvent Effect on Antimicrobial Hydrophilic Xerogel Coating of Medicinal Leathers in Simulated Industrial Finishing Process," *ChemPlusChem* 90, no. 5 (2025): e202400648, https://doi.org/10.1002/cplu.202400648.

15. C. Lin, Y. Chu, F. Liu, and P. Wang, "Study on Antibacterial Lubricating Coatings for Oral Implants Based on Electrostatic Self-Assembly and Schiff Base Reaction," *Colloids and Surfaces B: Biointerfaces* 259 (2025): 115343, https://doi.org/10.1016/j.colsurfb.2025.115343.

16. C. Lin, H. Yuan, and C. Wang, "The Study of Quantitative Friction-Damage Models at the Interventional Catheter-Vascular Tissues Interface," *Friction* (2025), https://doi.org/10.26599/frict.2025.9441194.

17. C. Lin, H. Yuan, and C. Wang, "Study on Lubricating Nano-Coatings for Cardiovascular Catheters Based on Molecular Self-Assembly and Schiff Base Reaction," *Friction* (2025), https://doi.org/10.26599/frict.2025.9441201.

18. W. Song, Z. Liu, Q. Li, et al., "Research on the Friction-Damage Mechanism Between Magnetic Guide Strip and Tracheal Tissue for Magnetic Navigation," *Tribology International* 215 (2025): 111487, https://doi.org/10.1016/j.triboint.2025.111487.

19. F.-C. Felipe, A. R. Manuel, P.-P. Patricia, et al., "Biocide Exposure in Extended-Spectrum β-Lactamase-Producing Klebsiella Pneumoniae: Effect on Increased Biocide and Antibiotic MICs, Genetic Changes, and Fitness Cost," *Journal of Applied Microbiology*, no. 6 (2025): 6, https://doi.org/10.1093/JAMBIO/LXAF121.

20. H. Ishii, T. Ikuno, A. Shimojima, and T. Okubo, "Preparation of Core–Shell Mesoporous Silica Nanoparticles With Bimodal Pore Structures by Regrowth Method - ScienceDirect," *Journal of Colloid and Interface Science* 448 (2015): 57–64, https://doi.org/10.1016/j.jcis.2015.01.057.

21. A. Ponnusamy, "Thermally Triggered Drug Delivery by Polyhedral Oligomeric Silsesquioxane Co -Conjugated With Gold as a Nano-Drug Carrier in Cancer Therapy," *Journal of Medical Science and clinical Research* 12, no. 1 (2024): 80–94, https://doi.org/10.18535/jmscr/v12i01.13.

22. J. Pu, X. Peng, R. Liu, et al., "Influence of Inflammatory Environment on the Fretting Corrosion of CoCrMo–Ti6Al4V Alloy Pairs at the Hip Head–Neck Interface," *Tribology International* 219 (2026): 111793, https://doi.org/10.1016/j.triboint.2026.111793.

23. J. Pu, Z. Zhang, Y. Zhang, et al., "Fretting-Corrosion Mechanisms of Ti6Al4V Against CoCrMo in Simulated Body Fluid Under Various Fretting States," *Friction* 12, no. prepublish (2024): 1–19, https://doi.org/10.1007/s40544-024-0909-0.

24. J. Pu, C. Liu, Y. Si, W. Cui, C. Zhang, and J. Song, "Tribocorrosion of Metallic Biomaterials Under Simulated Inflammation Conditions: Current Status and Future Prospects," *Advanced Healthcare Materials* 15, no. 7 (2025): e02419, https://doi.org/10.1002/adhm.202502419.

25. H. Yuan, C. Lin, and C. Wang, "Research Progress of the Interaction Between Blood Vessels and Intervention Catheters and Its Surface Modification," *Friction* 13, no. 7 (2025): 9441003, https://doi.org/10.26599/frict.2025.9441003.

26. W. Guo, L. Zhao, Z. Qin, Y. Wang, and H. Zhang, "Bioinspired Self-Adhesive Coating for Surface Functionalization of Medical Devices With Lubrication and Antibacterial Properties," *Friction* 13, no. 11 (2025): 9440926, https://doi.org/10.26599/frict.2025.9440926.

27. Y. Jia and H. Zhang, "A Hydrophilic Lubricating Coating With Dual Functions of Antibacterial Adhesion and Urease-Responsive Bactericidal Activity for Urinary Tract Implantable Devices," *ACS Applied Materials and Interfaces* (2025), https://doi.org/10.1021/ACSAMI.5C07616.

28. Y. Zhao, Z. Sun, G. Qiao, et al., "Microstructure Evolution of Alite In-Situ Carbonated by Aminated Mesoporous Silica Nanoparticles,"

Construction and Building Materials (November 2024): 453, https://doi.org/10.1016/J.CONBUILDMAT.2024.139052.

29. L. S. Lee, C. R. Chen, and C. W. Wu, "Feasible Fabrication of Chitosan Capped Mesoporous Silica Nanoparticles as a Smart Mucoadhesive Drug Delivery Platform for Dexamethasone for Long Term Lung Treatment," *Journal of Materials Science and Chemical Engineering* 13, no. 8 (2025): 20–85, https://doi.org/10.4236/msce.2025.138006.

30. S. K. Usul, A. Aslan, and B. E. Luleci, and B. Ergüden, "Effects of Hexagonal Boron Nitride and Mesoporous Silica Nanoparticles on the Morphology, Mechanical Properties and Antimicrobial Activity of Dental Composites," *Journal of Cluster Science* 35, no. 7 (2024): 2293–2309, https://doi.org/10.1007/s10876-024-02658-1.

31. N. Babers, M. G. D. El-Sherbiny, M. K. El-Shazly, and M. Bahaa, "Mechanical and Antibacterial Properties of Hybrid Polymers Composite Reinforcement for Biomedical Applications," *Journal of Biomaterials Science* 35, no. 1/3 (2024): 85–108, https://doi.org/10.1080/09205063.2023.2268949.

32. S. R. Maya, M. R. Posada, J. A. L. Rodas, et al., "Microstructural and Tribological Properties of TiO_2/Ag Multilayer Coatings Using Magnetron Sputtering Technique for Potential Applications in Non-Permanent Implants," *Thin Solid Films: An International Journal on the Science and Technology of Thin and Thick Films* (2024): 789, https://doi.org/10.1016/j.tsf.2023.140168.

33. L. Arda, Z. Raad, S. Veziroglu, C. Tav, and U. Yahsi, "The Influence of Defects on the Structural, Optical, and Antibacterial Properties of Cr/Cu Co-Doped ZnO Nanoparticles," *Journal of Molecular Structure* 1320 (2025): 139663, https://doi.org/10.1016/j.molstruc.2024.139663.

34. M. D. Garrido, B. Hamawandi, J. F. Serrano-Claumarchirant, et al., "A Rapid Synthesis of Magnetic-Core Mesoporous Silica-Shell Nanostructures—As Potential Theranostic Agents—By Means of Microwave Irradiation and the Atrane Method," *Nanoscale* 17, no. 11 (2025): 6539–6549, https://doi.org/10.1039/d4nr04572f.

35. Q. Xu, Y. Wang, Y. Zheng, et al., "Polymersomes in Drug Delivery—From Experiment to Computational Modeling," *Biomacromolecules* 25, no. 4 (2024): 2114–2135, https://doi.org/10.1021/ACS.BIOMAC.3C00903.

36. F. O. Kirbay and D. Odaci, "Electrospun Poly-ε-Caprolactone/Poly-L -Lysine (PCL/PLL) Nanofibers as an Emergent Material for the Preparation of Electrochemical Immunosensor to Detect Serum Amyloid A," *ACS Applied Polymer Materials* 6, no. 7 (2024): 3778–3786, https://doi.org/10.1021/acsapm.3c03002.s001.

37. J. Kotyńska and M. Naumowicz, "Monitoring Changes in the Zeta Potential and the Surface Charge of Human Glioblastoma Cells and Phosphatidylcholine Liposomes Induced by Curcumin as a Function of pH," *Chemico-Biological Interactions* 402 (2024): 111215, https://doi.org/10.1016/j.cbi.2024.111215.

38. S. Taheri, M. M. Heravi, and A. Saljooqi, "Ionothermal Synthesis of Magnetic N-Doped Porous Carbon to Immobilize Pd Nanoparticles as an Efficient Nanocatalyst for the Reduction of Nitroaromatic Compounds," *Scientific Reports* 13, no. 1 (2023): 17566, https://doi.org/10.1038/s41598-023-35998-5.

39. I. Siora, L. Andriyko, I. Gerashchenko, et al., "Comparative Study of the Structural Characteristics and Adsorption Capacity of Natural and Synthetic Zeolites," *Microporous and Mesoporous Materials* 397 (2025): 113778, https://doi.org/10.1016/j.micromeso.2025.113778.

40. F. Massahi Khosrowshahi, B. Ebrahimi-Hosseinzadeh, and A. Hatamian-Zarmi, "Sumac (Rhus coriaria) Extract Loaded-Mesoporous Silica Nanoparticle Efficiently as a Controlled Drug Delivery System for the Treatment of Atherosclerosis," *Journal of Inorganic and Organometallic Polymers and Materials* 34, no. 2 (2024): 793–803, https://doi.org/10.1007/s10904-023-02865-9.